ARTICLE

Controlling the Infrared Dielectric Function through Atomic-Scale Heterostructures

Daniel C. Ratchford,[†,◆] Christopher J. Winta,[‡,◆] Ioannis Chatzakis,[§] Chase T. Ellis,[†] Nikolai C. Passler,[‡] Jonathan Winterstein,[†] Pratibha Dev,[⊥] Ilya Razdolski,[‡,¶] Joseph R. Matson,[#] Joshua R. Nolen,[#] Joseph G. Tischler,[†] Igor Vurgaftman,[†] Michael B. Katz,[□] Neeraj Nepal,[†] Matthew T. Hardy,[†] Jordan A. Hachtel,[▲] Juan-Carlos Idrobo,[▲] Thomas L. Reinecke,[†] Alexander J. Giles,[†] D. Scott Katzer,[†] Nabil D. Bassim,[†,○] Rhonda M. Stroud,[†] Martin Wolf,[‡] Alexander Paarmann,*[‡] and Joshua D. Caldwell*[†,#]

†U.S. Naval Research Laboratory, Washington, D.C. 20375, United States
‡Physikalische Chemie, Fritz-Haber-Institut der MPG, Faradayweg 4-6, 14195 Berlin, Germany
§ASEE Postdoctoral Associate, U.S. Naval Research Laboratory, Washington, D.C. 20375, United States
⊥Department of Physics and Astronomy, Howard University, Washington, D.C. 20059, United States
¶FELIX Laboratory, Faculty of Science, Radboud University, 6500 GL Nijmegen, The Netherlands
#Department of Mechanical Engineering, Vanderbilt University, 2400 Highland Avenue, Nashville, Tennessee 37212, United States
□NRC Postdoctoral Associate, U.S. Naval Research Laboratory, Washington, D.C. 20375, United States
▲Center for Nanophase Materials Science, Oak Ridge National Laboratory, Oak Ridge, Tennessee 37831, United States
○Department of Materials Science and Engineering, McMaster University, Hamilton, Ontario JHE 357, Canada

S *Supporting Information*

ABSTRACT: Surface phonon polaritons (SPhPs), the surface-bound electromagnetic modes of a polar material resulting from the coupling of light with optic phonons, offer immense technological opportunities for nanophotonics in the infrared (IR) spectral region. However, once a particular material is chosen, the SPhP characteristics are fixed by the spectral positions of the optic phonon frequencies. Here, we provide a demonstration of how the frequency of these optic phonons can be altered by employing atomic-scale superlattices (SLs) of polar semiconductors using AlN/GaN SLs as an example. Using second harmonic generation (SHG) spectroscopy, we show that the optic phonon frequencies of the SLs exhibit a strong dependence on the layer thicknesses of the constituent materials. Furthermore, new vibrational modes emerge that are confined to the layers, while others are centered at the AlN/GaN interfaces. As the IR dielectric function is governed by the optic phonon behavior in polar materials, controlling the optic phonons provides a means to induce and potentially design a dielectric function distinct from the constituent materials and from the effective-medium approximation of the SL. We show that atomic-scale AlN/GaN SLs instead have multiple Reststrahlen bands featuring spectral regions that exhibit either normal or extreme hyperbolic dispersion with both positive and negative permittivities dispersing rapidly with frequency. Apart from the ability to engineer the SPhP properties, SL structures may also lead to multifunctional devices that combine the mechanical, electrical, thermal, or optoelectronic functionality of the constituent layers. We propose that this effort is another step toward realizing user-defined, actively tunable IR optics and sources.

KEYWORDS: *surface phonon polaritons, polar semiconductor, infrared, superlattice, second harmonic generation, optic phonons, interface phonon*

AlN/GaN superlattice
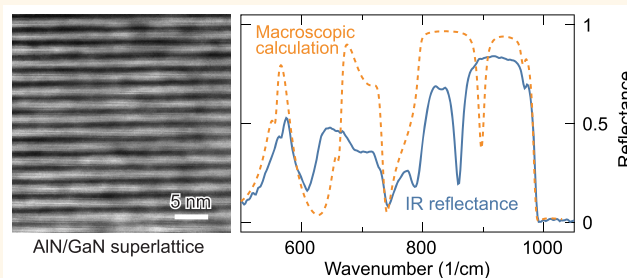
The mid-infrared (MIR) to terahertz (THz) spectral region offers great potential for technological advancement using nanophotonics, which can impact numerous applications including super-resolution imaging,[1−4]

enhanced spectroscopy,[5] and narrow-band optical sources[6] as well as free-space signaling and communications.[7] For instance, nanophotonic approaches are well suited for sensing trace levels of chemical species through enhanced vibrational fingerprinting,[8,9] owing to molecular vibrational frequencies in this spectral range. One promising avenue for realizing these technologies is to use surface phonon polaritons (SPhPs), which greatly enhance light-matter interactions by confining light to subdiffractional dimensions at the surface of a polar material.[4,10−16] SPhPs are supported between the transverse (TO) and longitudinal optic (LO) phonon frequencies of polar dielectrics, that is, within the so-called Reststrahlen band, through the coupling of incident light with the oscillating ionic charges on the polar lattice.[12] One significant benefit of SPhPs is the substantially reduced losses they exhibit in comparison to surface plasmon polaritons (SPPs). This is the result of the fast scattering of electrons in metals and semiconductors compared to the much longer scattering times associated with optic phonons.[17] Since the intrinsic losses of SPPs have limited their broad application in many practical devices, low-loss SPhPs offer a highly attractive alternative.[12,18,19]

One of the most important technological hurdles for the implementation of SPhPs in nanophotonic and metamaterial technologies is that once a polar material is chosen, the spectral characteristics of the SPhPs it supports are fixed.[20] While there are many polar materials that occur in nature featuring Reststrahlen bands that combine to cover the entire MIR to THz spectral domain,[21] any given material will only support SPhPs within its own relatively narrow specific band. Here, we experimentally demonstrate an approach for broadening the spectral range of the SPhPs by using atomic-scale superlattices (SLs) composed of commercially established polar semiconductors. When materials are combined into SLs, the SL vibrational modes are modified from that of the bulk phonons of the constituent materials by interfacial chemical bonding, electrostatic effects, and changes to the material lattice constants.[22,23] Confinement effects can arise, resulting in confined phonon modes that oscillate predominantly in one material,[22] or new vibrational states can occur that feature phonons redistributed over both materials. Interface phonon modes may also be supported, wherein the vibration is localized to the interfaces between the constituent materials.[24] In addition, significant strain can develop in such atomic-scale SLs, resulting in controllable spectral shifts in the phonon frequencies. As the SL layer thickness is reduced down to a length scale approaching a few monolayers, chemical bonding between the interfacial layers plays an increasingly prominent role in determining the phonon modes in the SL. These phonon modes, in turn, have a direct impact on the SL dielectric function. We refer to such atomic-scale SL structures where the IR dielectric function diverges from its constituents as a crystalline hybrid (XH)[20,25] since it is these changes to the chemical structure of the crystal lattice that modify the IR response.

We demonstrate the XH approach by using atomic-scale AlN/GaN SLs, which exhibit a highly anisotropic IR response featuring multiple Reststrahlen bands. Using second harmonic generation (SHG) phonon spectroscopy, we probe the SL phonon modes and identify multiple confined phonons. We further show that the phonon modes, which define the upper and lower limits of the Reststrahlen bands, shift by >10 cm^{-1} depending on the SL layer thicknesses. By extracting the SL dielectric function via IR ellipsometry, we further illustrate that

the SL has spectral regions that support surface-confined SPhPs as well as volume-confined hyperbolic phonon polaritons (HPhPs). In spectral ranges where hyperbolicity is present, the spectral dispersion in both the negative and positive permittivity directions is quite strong, in stark contrast to typical natural hyperbolic materials[11,13,26] and hyperbolic metamaterials.[27] Our results are corroborated by density-functional perturbation theory (DFPT) calculations of the SL vibrational patterns, which show the characteristics of confined and interface modes as well as those of hybrid modes that do not resemble any established profile in macroscopic theory. The XH approach therefore provides the opportunity to modify the optic phonon frequencies, the dielectric function and dispersion of the optical constants, as well as the width of the Reststrahlen bands. Therefore, with more extensive investigations into the XH design principles, we envision the ability to create engineered materials for IR and THz nanophotonics and optoelectronics, incorporating additional functionalities through appropriate material selection.

RESULTS AND DISCUSSION

To demonstrate the XH concept, multiple AlN/GaN SL samples, each with layer thicknesses of ~10 or fewer monolayers, were grown along the wurtzite c-axis using molecular beam epitaxy (MBE). A representative schematic of the layered sample configuration is provided in Figure 1a for an AlN/GaN SL grown on a SiC semi-insulating substrate. Wurtzite GaN and AlN are both birefringent with $A_1(TO)$ and $A_1(LO)$ phonon modes that oscillate parallel to the crystal c-axis and $E_1(TO)$ and $E_1(LO)$ phonon modes that oscillate perpendicular to the c-axis. For GaN (AlN), these bulk phonon frequencies[28,29] are $A_1(TO)$ = 533 (614) cm^{-1}, $A_1(LO)$ = 735 (893) cm^{-1}, $E_1(TO)$ = 561 (673) cm^{-1}, and $E_1(LO)$ = 743 (916) cm^{-1}. In bulk form, AlN and GaN have a similar IR response, with partially overlapping Reststrahlen bands bound by their respective optic phonon frequencies. This is shown in Figure 1b, which plots the calculated reflectance of bulk GaN (blue), AlN (orange), and SiC (red).

Two representative SL structures, referred to as Samples 'A' and 'B', are discussed here. Sample A, shown in the cross-sectional scanning transmission electron microscope (STEM) image in Figure 1c, consists of 50 alternating layers of AlN and GaN grown on a ~50 nm thick AlN buffer layer. Since this sample was deliberately not rotated during growth, a gradient in the Al- and Ga-flux across the wafer surface resulted in a strong variation in the corresponding layer thicknesses, with values ranging from 2 to 3 nm for the AlN and GaN layers depending on the position on the sample. At the particular location displayed in Figure 1c, each layer is ~2 nm thick. Sample B (STEM image in Figure 1e) consists of a SL with 500 atomically thin, alternating layers of AlN and GaN with thicknesses of ~1.2 nm (~4 monolayers) and ~1.4 nm (~5 monolayers), respectively. The layer thicknesses in Sample B are much more uniform across the sample surface, which result from the sample rotation performed during growth. The STEM and X-ray diffraction (XRD) measurements imply chemical intermixing at the interfaces, and that the SLs are partially relaxed, but with an overall high degree of chemical segregation (see Sec. S3 in the Supporting Information).

The optic phonon modes of SLs consisting of polar materials[30] including III-nitride materials systems[31−36] have been extensively studied and generally described using both microscopic and macroscopic models.[24] For sufficiently thick
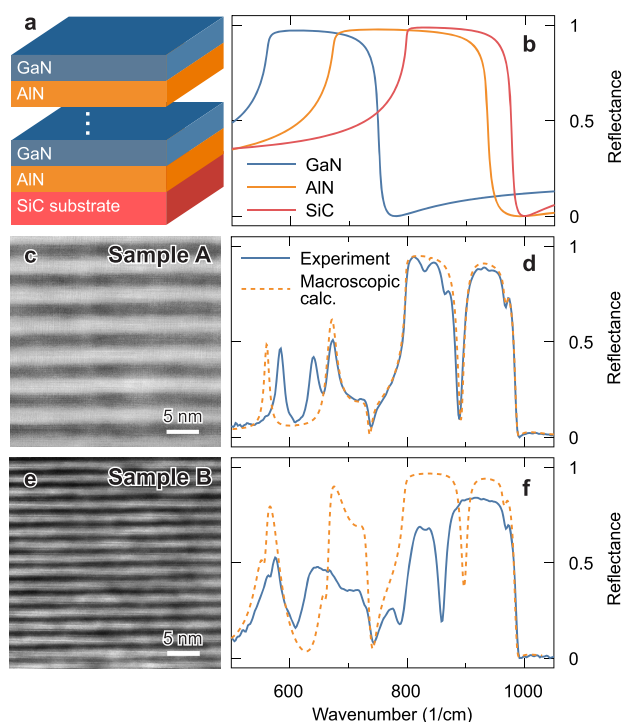
Figure 1. STEM images and reflectance spectra of AlN/GaN heterostructures and Reststrahlen bands. (a) Illustration depicting AlN/GaN heterostructures. (b) Calculated reflectance spectra of bulk GaN, AlN, and SiC for normal incidence light in the IR, showing the spectral overlap of the Reststrahlen bands. (c, e) Cross-sectional high-angle annular dark-field STEM images of AlN/GaN heterostructures with AlN (GaN) thicknesses of ~2.2 nm (2.2 nm) for Sample A and ~1.2 nm (1.4 nm) for Sample B, respectively. The AlN layers appear as dark-gray bands, and the GaN layers as light-gray bands. (d, f) Measured reflectance spectra (blue line) at an incidence angle of 65° and the calculations (orange dashed lines) based on the bulk properties of the AlN/GaN SL from panels c and e, respectively.

layers, it is accepted that the effect of the phonon modes on the SL IR response can be described using macroscopic electromagnetic modeling, for example, the transfer-matrix method, starting from the bulk permittivity of each layer.[37] A particularly simple macroscopic approximation that applies when the SL layers are much thinner than the wavelength of the light within the materials is the well-known effective-medium theory. However, as the layer thicknesses in the SL are reduced to just a few atomic layers, the SL phonon modes are no longer well described by such macroscopic models. This is because atomic-scale interactions modify the SL phonon modes, namely, the prominent effects of the interface bonds impose different boundary conditions, and the lattice constants of the epitaxially grown layers deviate from bulk values. This point is illustrated in Figure 1d and f, where the measured IR reflectance (blue line) is plotted for Samples A and B, respectively, along with the calculated reflectance (orange dotted line) of the SLs using the transfer-matrix method based on the bulk optical constants of AlN and GaN. It is clear that the conventional approach toward predicting the IR reflectance fails, due to the strong quantitative mismatch of peak positions and the emergence of additional spectral features in the experimental spectra. It is even less accurate for Sample B that

features thinner layers and hence exhibits more prominent interface and confinement effects.

In an effort to quantify the impact of the SL design, we first characterize the SL optic phonons, which define the poles and zeros of the IR dielectric function, and the spectral extent of the Reststrahlen bands. Quantitative analysis of the phonon modes from FTIR spectra is difficult due to the highly reflective nature of the Reststrahlen band of the SiC substrate, along with the high reflectance of the developing XH Reststrahlen bands located between the multiple LO/TO phonon pairs. Thus, we employed IR SHG,[38−42] collecting spectra from the AlN/GaN SL using the IR emission from a free-electron laser.[43] This technique was recently shown to provide clear identification of phonon modes in multimode systems[44] since it allows the direct measurement of phonon peaks on a nominally flat spectral background.

IR SHG and reflectance spectra were collected from three locations on Sample A with varying AlN and GaN layer thicknesses and are shown in Figure 2a and b, respectively.
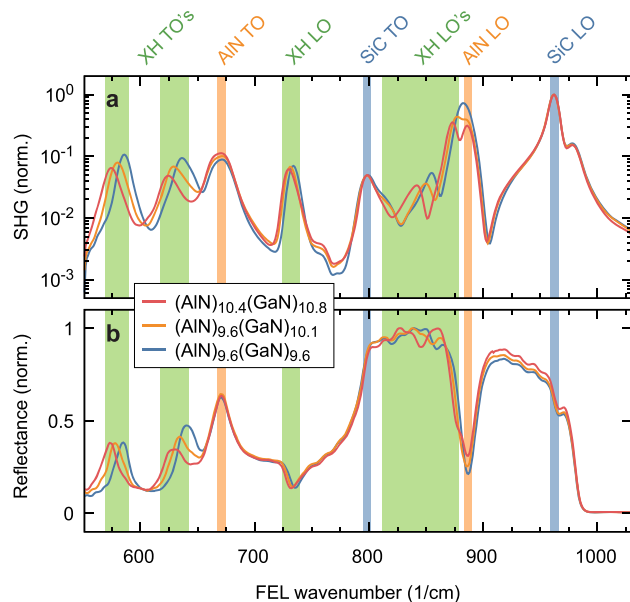

Figure 2. Modification of optic phonons in the XH structure of Sample A. (a) Experimental SHG spectra at three selected positions on the SL with graded AlN and GaN layer thicknesses. Subscripts in the legend denote the average number of monolayers. SHG peaks marking the SL's optic phonon modes shift spectrally with varying layer thicknesses, thus demonstrating the ability to design the XH modes (green shade). In contrast, SHG peaks at AlN and SiC bulk phonon frequencies (orange and blue shade, respectively) originating from the buffer layer and the substrate, respectively, do not shift as the SL's layer thicknesses vary. (b) Corresponding reflectance spectra. The layer-thickness-dependent behavior of the XH optic phonons in the linear response is consistent with the features observed in the SHG spectra. Please note the logarithmic scale in panel a.

Within the SHG spectra, each $E_1(TO)$ phonon is observed with large contrast.[44] Additionally, $A_1(LO)$ phonons of the SL can be closely approximated via the Berreman effect,[45] which produces subtle dips in the reflectance near the spectral position where the real part of the permittivity crosses through zero (the so-called epsilon-near-zero condition). The strong confinement of the electromagnetic fields of the Berreman modes[46,47] also results in pronounced peaks in the SHG

Table 1. Calculation of Biaxial Strain in GaN and AlN Layers at Sample Locations Corresponding to Red, Orange, and Blue Curves in Figure 2[a]

	GaN				AlN			
curve	ε_{xx}^{RSM} (%)	E_1(TO) (cm^{-1})	σ_{xx} (GPa)	ε_{xx}^{SHG} (%)	ε_{xx}^{RSM} (%)	E_1(TO) (cm^{-1})	σ_{xx} (GPa)	ε_{xx}^{SHG} (%)
red	−1.2 (1)	585.9 (1)	−6.9 (6)	−1.4 (1)	1.3 (1)	637.6 (1)	7.8 (4)	1.5 (1)
orange	−1.0 (1)	580.2 (1)	−5.3 (6)	−1.1 (1)	1.4 (1)	631.5 (1)	9.1 (4)	1.8 (1)
blue	−0.7 (1)	574.7 (1)	−3.8 (6)	−0.8 (1)	1.8 (1)	625.6 (1)	10.4 (4)	2.0 (1)

[a]ε_{xx}^{RSM} is the in-plane strain determined by X-ray diffraction reciprocal space mapping. σ_{xx} and ε_{xx}^{SHG} are the biaxial stress and in-plane strain estimated from the frequency shift of the E_1(TO) phonon modes in Figure 2. Error of the last digit is denoted in the parentheses.

spectra.[48] In addition to the phonon resonances of the SL, those corresponding to the SiC substrate and AlN buffer layer are also present in the spectra (Figure 2a). However, these two sets of modes are easily identified, as they occur at the bulk TO and LO phonon frequencies of these materials and do not vary spectrally with the changing layer thicknesses at different positions on the wafer surface. The SHG peaks originating from the SiC, the AlN buffer, and the SL are highlighted in blue, orange, and green, respectively, in Figure 2. From these measurements, the thickness-dependent spectral dispersion of the SL IR modes can be identified.

The modification of the phonons in the XH can be quantified through line shape analysis of the SHG spectra. The SL is observed to support two E_1(TO)-like phonon modes around ∼575 cm^{-1} and ∼630 cm^{-1} as well as three A_1(LO)-like phonons: one at ∼735 cm^{-1} and two more at ∼840 and 880 cm^{-1}. From the SHG spectra, it is clear that the spectral positions of the SL optic phonons vary strongly across the wafer (see Sec. S4 and Figure S4 in the Supporting Information for the full data set and extended discussion). We observe significant frequency shifts (>10 cm^{-1}) of these modes even for small, angstrom-scale changes in the layer thicknesses. One possible explanation for such strong sensitivity of the phonon frequency to the layer thickness is the potential variation in lattice strain across the wafer. Lattice strain has been shown to produce shifts in the phonon frequencies in AlN/GaN SLs.[31,49] The lattice mismatch between AlN (in-plane lattice constant a = 3.112 Å) and GaN (a = 3.189 Å) is ∼2.5%; therefore, we expect a significant modification of the lattice constants of the SL, with the in-plane values falling between those of AlN and GaN. This results in tensile and compressive strain for the AlN and GaN layers, respectively. In this case, the effective in-plane lattice constant in the structure should strongly depend upon the thickness ratio between the two materials. We used high-resolution XRD reciprocal space mapping (RSM) to measure the in-plane lattice constants of the constituent layers and determine the in-plane strain. The in-plane lattice constant was measured to be 3.152 Å, 3.157 Å, and 3.168 Å for the sample positions corresponding to the red, orange, and blue curves in Figure 2, respectively. In Table 1, we report the in-plane strain ε_{xx}^{RSM} for the AlN and GaN layers with these lattice constants relative to the corresponding bulk in-plane lattice parameters (3.112 and 3.189 Å, respectively). The biaxial strain in the GaN (AlN) layers varies from −0.7 to −1.2% (1.3 to 1.8%).

To determine if the observed phonon shifts can be the result of the measured lattice strain in the SLs, we estimated the in-plane lattice strain necessary to cause the observed phonon spectral shifts in Figure 2. The E_1(TO)-like phonon frequencies around ∼575 cm^{-1} and ∼630 cm^{-1} in Figure 2 are similar to the corresponding frequencies of bulk GaN (∼561 cm^{-1}) and AlN (∼673 cm^{-1}), respectively. In addition,

the A_1(LO)-like phonons at ∼735 and 880 cm^{-1} are close in frequency to the A_1(LO) frequencies of bulk GaN (∼735 cm^{-1}) and AlN (∼900 cm^{-1}), respectively. This suggests that these SL phonon modes correspond to GaN-like and AlN-like E_1(TO) and A_1(LO) modes that are spectrally shifted due to strain. We calculated the biaxial stress σ_{xx} in the AlN and GaN layers using the shift of the E_1(TO) phonon frequencies relative to the bulk values in unstrained GaN and AlN and the pressure coefficients for GaN and AlN.[50,51] The results are summarized in Table 1. We also calculated the in-plane strain ε_{xx}^{SHG} for the GaN and AlN layers using the following equation:

$$\varepsilon_{xx} = \left(C_{11} + C_{12} - 2\frac{C_{13}^2}{C_{33}} \right)^{-1} \sigma_{xx} \tag{1}$$

where C_{ij} represents the elastic constants for GaN or AlN.[29,31,52] The strain necessary to generate the observed spectral shifts is consistent with the strain measured using RSM. Therefore, controlling the AlN/GaN layer thicknesses provides a direct means to tune the phonon frequencies through lattice strain, which depends on the thickness ratio between AlN and GaN. In addition to strain, the layer thicknesses can potentially influence the phonon frequencies through interface bonding and abruptness, bond lengths with the layers, and phonon confinement. Understanding the impact of these variables on the phonon frequencies and corresponding influence upon the IR dielectric function of XH materials will be the focus of subsequent work.

It is apparent from the presence of additional phonon modes and larger spectral shifts in the phonon spectrum of the atomic-scale SL in Sample B (Figure 1f) that a description of the modified dielectric function using only strain-induced shifts of the bulk optic phonon modes is incomplete. As the SLs are reduced to just a few atomic layers, the effects of the modified chemical bonding at the interfaces become more prominent. To identify the origin of these new SL-specific phonon modes, we turn to DFPT,[23] which provides a direct and powerful means of incorporating the atomistic details (i.e., the effects of the interface bonds and modified lattice constants) on the XH phonon modes. We employ DFPT to calculate the phonon modes of Sample B with the assumption that it has five monolayers of GaN and four monolayers of AlN in each period (close to the measured layer thicknesses from the cross-sectional TEM analysis) as well as fully relaxed lattice constants. A full list of the resultant phonon modes is presented in Table S3 of the Supporting Information.

To compare the DFPT calculation with the IR response of Sample B, we extracted the XH dielectric function from IR ellipsometric spectra. For these XH structures, where the layer thicknesses are only a few monolayers, interfacial bonding plays a significant role in shaping the phonon density of states. To account for this effect, we treat the XH structure as a whole
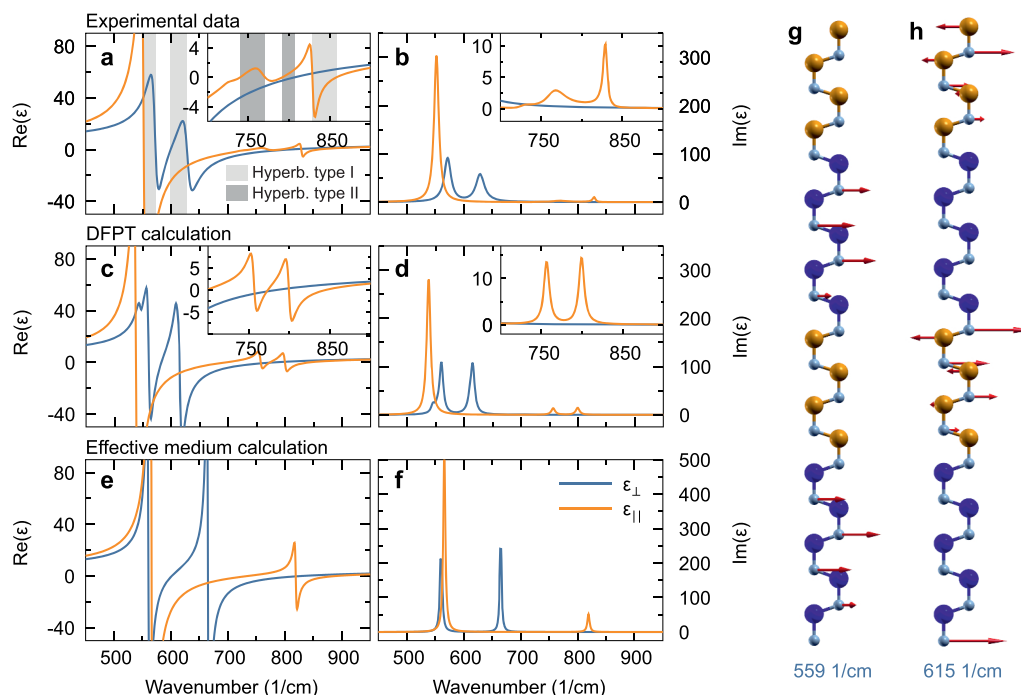
Figure 3. Dielectric function of the atomic-scale AlN/GaN SL. (a, b) Measured, (c, d) calculated using DFPT, and (e, f) calculated using effective-medium theory real and imaginary parts of the dielectric function of the AlN/GaN SL (Sample B). The in-plane component, $\varepsilon_\perp$, and the out-of-plane component, $\varepsilon_\parallel$, are shown in blue and orange, respectively. Highlighted areas in panel a mark the hyperbolic regions of type I (light gray) and type II (dark gray). (g, h) Phonon vibrational patterns associated with the 559–583 cm^{-1} and 615–784 cm^{-1} Reststrahlen bands, respectively, for $\varepsilon_\perp$ shown in panel c. Blue, orange, and gray spheres denote Ga, Al, and N, respectively, and red arrows denote atomic displacement.

and derive a dielectric function for the entire layer. The AlN/GaN XH is strongly birefringent, with very different in-plane and out-of-plane dielectric responses, denoted $\varepsilon_\perp$ and $\varepsilon_\parallel$, respectively. The dielectric function for a polar semiconductor with k phonon modes is given by

$$\epsilon(\omega)_j = \epsilon_{\infty,j} \prod_k \left(1 + \frac{\omega_{\text{LO}k,j}^2 - \omega_{\text{TO}k,j}^2}{\omega_{\text{TO}k,j}^2 - \omega^2 - i\omega\gamma_{k,j}} \right) \tag{2}$$

where $j = \parallel$ or $\perp$ for the permittivity parallel or perpendicular to the c-axis.[53] The parameter ϵ_∞ is the high frequency dielectric constant, and ω_{LO} and ω_{TO} are the LO and TO phonon frequencies, with a damping parameter of γ. The $\omega_{\text{TO},\parallel}$ and $\omega_{\text{LO},\parallel}$ phonon modes with A_1 symmetry oscillate parallel to the c-axis, while the $\omega_{\text{TO},\perp}$ and $\omega_{\text{LO},\perp}$ phonons with E_1 symmetry oscillate perpendicular to the c-axis. We extracted the dielectric function of the SL from Sample B (Figure 3a,b) through least-squares fitting of IR ellipsometry data, using eq 2 as the fitting function and the WVASE program from J.A. Woollam.[54] However, as spectroscopic ellipsometry is insensitive to the $A_1(\text{TO})$ mode for a basal-plane oriented uniaxial crystal,[35,49] the frequencies of the $A_1(\text{TO})$ mode was determined separately using confocal Raman spectroscopy and fixed as 552 cm^{-1} in the ellipsometric fit. We also used eq 2 to calculate the dielectric function using the DFPT-derived phonon modes (Figure 3c,d). For this dielectric function, the damping parameter was empirically chosen to be 10 cm^{-1} for all phonon modes. For comparison, the effective-medium calculations of the XH dielectric function using the optical constants for bulk GaN and AlN measured by ellipsometry are also provided (Figure 3e,f). The effective-medium calculation

is based on the average of the GaN and AlN dielectric functions weighted by the relative thickness of the layers. It is clear that the effective-medium calculation fails to predict several important features of the IR response because it does not account for the atomic-scale interactions between the layers. On the other hand, good qualitative agreement with experiment is found with the DFPT-derived dielectric function. The small frequency shifts of the modes between the DFPT and experiment are typical and can be attributed to the choice of the exchange-correlation functional. The DFPT calculation accurately predicts multiple short-wavelength phonon modes for the out-of-plane permittivity induced by the reduced crystal symmetry of the SL. It can also provide physical insight into the qualitative vibrational character of the modes. Thus, the atomic-scale SL should be considered as a XH material, with a distinct dielectric function dictated by the atomic-scale interactions within the SL.

From the extracted XH dielectric function, it is found that Sample B exhibits multiple Reststrahlen bands (identified by regions with Re(ε) < 0) as a result of the induced and shifted optic phonon modes. The poles in the dielectric function occur at $E_1(\text{TO})$-like and $A_1(\text{TO})$-like phonon frequencies and the zero crossings near $E_1(\text{LO})$-like and $A_1(\text{LO})$-like phonon frequencies for $\varepsilon_\perp$ and $\varepsilon_\parallel$, respectively. The in-plane dielectric function $\varepsilon_\perp$ displays two Reststrahlen bands: one narrow region from 572 to 599 cm^{-1} and another from 629 to 807 cm^{-1}. Similar Reststrahlen bands occur in the dielectric function derived from the DFPT calculations (Figure 3c), but with a ~15 cm^{-1} redshift. The calculated phonon vibrational pattern associated with the 559–583 cm^{-1} Reststrahlen band (Figure 3g) illustrates that it most closely resembles a GaN-confined mode. In contrast, the vibrational
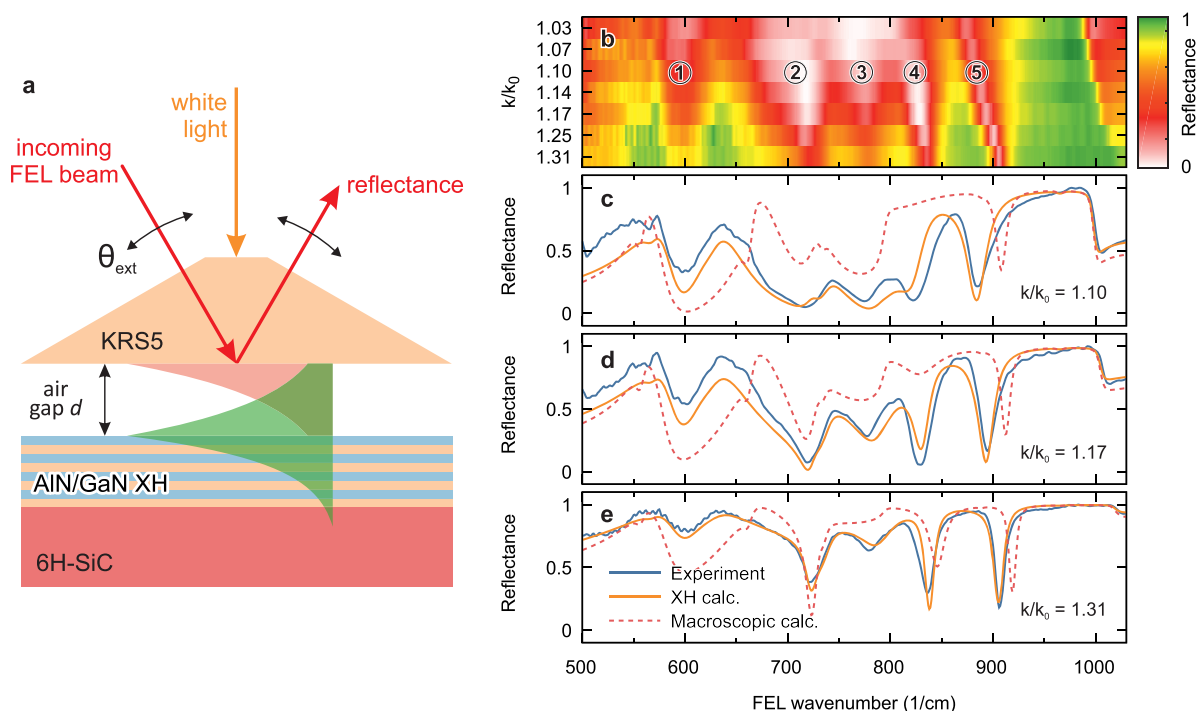
Figure 4. Experimental polariton dispersion of the XH. (a) Schematic of the Otto-type prism coupling experiment[40] that probes the dispersion of XH polaritons for wavevectors near the light line. Total internal reflection at the prism (KRS5, $n = 2.4$) backside launches evanescent waves (red shaded) with in-plane momenta k, tunable via the incidence angle θ_{ext}, that couple to evanescent modes in the XH (green shaded) across a well-defined air gap of thickness d determined by white-light interferometry.[60] (b) Experimental reflectance map for a series of normalized wavevectors k/k_0, where k_0 is the wavevector in vacuum, at fixed air gap thickness $d = 3.0~\mu$m. SPhP modes appear as minima (red−white shading). (c−e) Experimental (blue) and calculated (solid orange and dashed red) reflectance spectra for selected momenta.

characters associated with the phonons occurring at the phonon frequencies of the $615-784$ cm^{-1} Reststrahlen band (Figure 3h) are confined predominantly within the AlN layers but are centered at the AlN/GaN interface. Importantly, the in-plane Reststrahlen bands of the XH cover a broader range than that of GaN ($\sim561-743$ cm^{-1}) and are on the same scale as AlN ($\sim673-916$ cm^{-1}). To our knowledge, the only other way to achieve such broadening of the Reststrahlen band is through the inclusion of high densities of free carriers, for example, via doping.[55] However, this approach introduces substantial increases in loss due to the inclusion of free-carrier scattering, dopant scattering of optic phonons, and the increased Drude weight within the dielectric function. To put this in context, we estimate that shift of the Reststrahlen band of GaN out to 800 cm^{-1} via free carriers would require a carrier density of $\sim3 \times 10^{18}$ cm^{-3} and would increase Im(ε) by about six-fold at 800 cm^{-1}. In contrast, even within the nonoptimized XH structures discussed here with multiple interfaces and significant strain increased Im(ε) by about a factor of 3.

The out-of-plane dielectric function $\varepsilon_{\parallel}$ is dominated by a broad Reststrahlen band extending from ~536 cm^{-1} to ~740 cm^{-1}. Examination of the corresponding vibrational pattern from the DFPT calculation (Figure S10) shows that the phonon mode includes the displacement of nitrogen atoms in both layers. While the nitrogen atomic displacement is larger in the GaN layers, the phonon vibration exhibits an extended character. Two additional Reststrahlen bands are observed within $\varepsilon_{\parallel}$, with one extending from 769 to 791 cm^{-1} and the other from 828 to 859 cm^{-1}. Examination of the lattice

vibrational patterns indicates that these modes involve atomic movement in both layers, but a larger amplitude in the AlN due to its lighter reduced mass. The energy scale of the optic phonons is mostly driven by the lighter of the two atomic species in a diatomic lattice (here, nitrogen).[12] The small difference in the reduced masses of GaN (~11 amu) and AlN (~9 amu) results in a spectral overlap of the respective Reststrahlen bands and the limited degree of confinement of the SL phonon modes observed in these structures.

The strongly anisotropic Reststrahlen bands of the XH result in both elliptical (the same sign of $\varepsilon_{\perp}$ and $\varepsilon_{\parallel}$) and hyperbolic (opposite signs) behaviors within the long-wave IR.[27] However, unlike most hyperbolic systems studied to date, the vibrational resonances of the XH and the strong spectral dispersion result in a wide spectral range over which both the positive and negative permittivities vary rapidly with frequency. In the Supporting Information (Figure S7), we plot the birefringence, $\Delta n = n_e - n_o$, of Sample B, which is in excess of unity over a large portion of the spectral range. Because of the rapidly changing dispersion, Δn reaches a maximum of ~10 at 527 cm^{-1} but then drops to ~-8 at 566 cm^{-1}. Such extreme birefringence is about an order of magnitude larger than the recently reported materials of BaTiS$_3$ and MoO$_3$,[26,56,57] which exhibit birefringence values of about 0.76 and 0.31, respectively. This highlights an important opportunity to engineer hyperbolic spectral behavior through careful selection of the SL polar semiconductor constituents, thicknesses, and epitaxial mismatch.

One challenge associated with using atomic-scale SL designs to modify the IR dielectric function is to ensure the optical loss
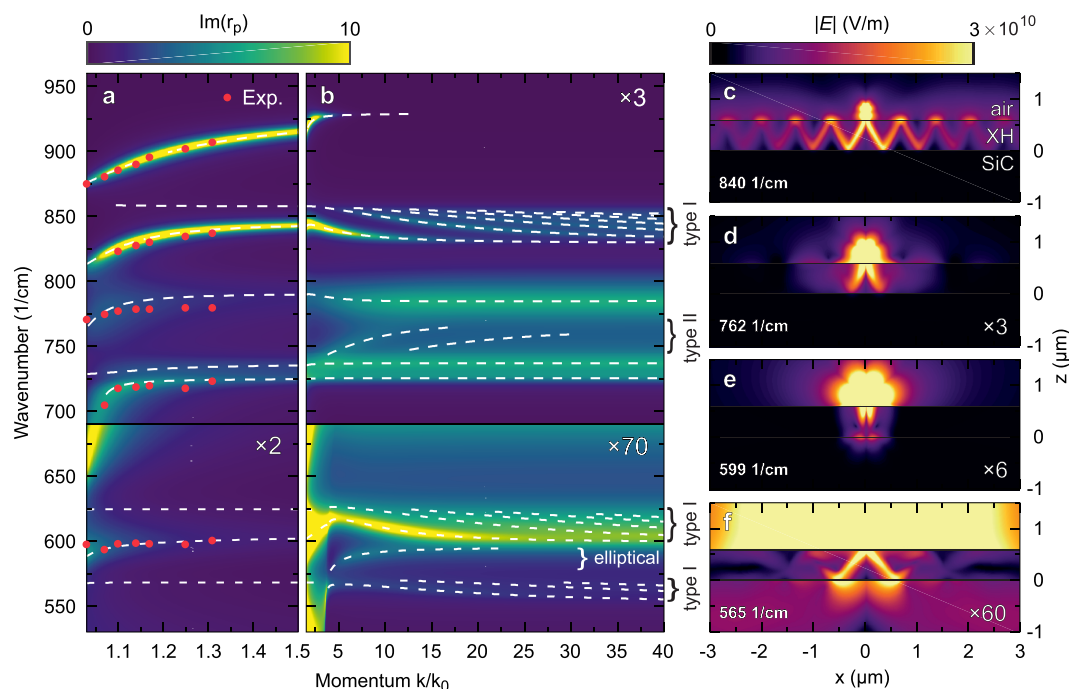
Figure 5. Theoretical polariton dispersion and strongly confined phonon polaritons of the XH. (a, b) Imaginary part of the Fresnel reflection coefficient for p-polarized light $\mathrm{Im}(r_p)$ of Sample B for evanescent wave excitation as a function of the relative in-plane momentum k/k_0. The dashed lines represent the modes extracted from calculations with reduced damping. The red dots in panel a mark the positions of the reflectance dips in the Otto geometry experiments. Hyperbolic mode progression is observed in b) for all four hyperbolic regions. Additionally, a strongly elliptical mode is observed as indicated. (c−f) Spatial electric field profiles for localized excitation of hyperbolic modes of (c, e, f) type I and (d) type II. The mode shown in panel e exhibits a rigid angle of propagation close to zero since here the positive dielectric tensor component $\varepsilon_\perp$ is nearly zero.

is not substantially increased. The loss can be quantified by comparing the damping parameter, γ, of the different modes of the XH to the bulk constituents, GaN and AlN. The damping parameters were extracted from the dielectric function fits for each of the XH phonon modes and are listed in Table S2 in the Supporting Information, with the values falling within the 10−25 cm^{-1} range. For comparison with the XH, we also grew films of bulk GaN and AlN and used ellipsometry to determine γ for the phonon modes. The extracted value of γ was ∼5 cm^{-1} for the GaN phonon modes and ∼15 cm^{-1} for the AlN modes. Therefore, the XH IR losses are on the order of the bulk constituents and thus can be modified without a dramatic rise in optical losses.

One test of the validity of the experimentally extracted XH dielectric function is to make accurate predictions of the polariton modes. To this end, we employed prism-coupling in the Otto geometry (see Methods for details),[40,58,59] which provides experimental access to the dispersion of the polariton modes for wave vectors near the light line, as shown in the schematic of Figure 4a. Because of the multimode nature of the XH, multiple polariton branches with different dispersions are observable. The experimental dispersion maps of the XH are shown in Figure 4b, where several dispersing polariton modes are clearly identified.

To corroborate the experimental findings with the XH concept, we calculated the polaritonic dispersion spectra for the Otto geometry using a transfer-matrix method for anisotropic materials.[37] Two complementary models were employed to describe the IR response of the SL structure: (i) the extracted XH dielectric function (Figure 3a,b) and (ii) an explicit calculation using the bulk dielectric functions for both

AlN and GaN thin layers. For very thin layers, the latter model is expected to produce results that are equivalent to the effective-medium theory. The results of the transfer matrix calculations for several cuts through the dispersion are shown along with the respective experimental spectra in Figure 4c−e. From these comparisons, we find very good agreement with the model (i) using the XH dielectric function (solid orange). In contrast, the multilayer calculations (ii) (dashed red) cannot reproduce the observed polaritonic response.

The experimental dispersion in Figure 4b suggests five distinct polariton branches. The highest-frequency mode arises from the SiC surface polariton that is strongly modified by the XH film. Notably, with the thickness of 585 nm of the XH film, this mode repulsion is well outside the strong-coupling regime[61,62] and should instead be understood as an effective index induced shift in the SiC SPhP response. The remaining four surface polariton branches arise from the XH film itself and are only mildly affected by the substrate as their penetration depth is comparable to, or smaller than the XH total thickness. To verify this mode assignment, we calculated the theoretical dispersion of the XH for different thicknesses and substrates, see Sec. S8 and Figures S11 and S12 in the Supporting Information for details. The results for Sample B are provided in Figure 5a and b, where we evaluated the imaginary part of the reflection coefficient r_p, which peaks at polariton resonances.[13] For small wavevectors shown in Figure 5a, multiple branches of strongly dispersing surface polaritons are visible, in excellent agreement with the positions of the reflectance dips extracted from the Otto geometry experimental data (Figure 4b−e).

Strongly confined hyperbolic and elliptical polariton modes of the XH emerge at larger wavevectors as shown in Figure 5b, as expected from the hyperbolic and elliptical regions of the XH dielectric function (Figure 3a). Notably, we observe three hyperbolic bands of type I (830−860 cm^{-1}, 599−625 cm^{-1}, 555−571 cm^{-1}), where only one crystal axis exhibits a negative real part of the dielectric function, which show the typical mode progression.[13] Additionally, we also observe one hyperbolic band of type II (two axes with negative permittivity; 740−770 cm^{-1}) and one elliptical band (all three axes negative; 572−599 cm^{-1}). As a consequence of the rapid dispersion of the XH dielectric tensor and its anisotropy, the properties of these polaritons vary strongly for the different Reststrahlen bands and even within each band. This is in stark contrast to other hyperbolic materials, where the respective positive component of the dielectric tensor is typically constant throughout the hyperbolic dispersion.[1,2,11,13] To illustrate this behavior, we calculated optical field profiles of polariton modes from the various branches, with representative examples shown in Figure 5c−f. The strong modulations of both components of the dielectric tensor result in hyperbolic modes whose rigid angle of propagation[63−65] and propagation length vary drastically with small spectral changes, see Figure S13 in the Supporting Information for a larger set of mode profiles.

Notably, the XH concept provides two independent tuning parameters of the polaritonic dispersion: (i) modification of the optic phonons through the individual atomic-scale layer thicknesses as demonstrated here, leading to modified number, positions, and widths of the polaritonic bands; (ii) the total SL stack thickness through the number of SL repeated layers changing the dispersion of the modes within each band. The latter is shown in Figure S12 in the Supporting Information, where we calculated the polaritonic dispersion for a series of XH total stack thicknesses. Therefore, the XH concept provides numerous opportunities for super-resolution imaging and nanolithography[3,4] with increased spectral flexibility.

An additional major benefit of the XH approach is that it allows for the combination of two materials to achieve a desired IR response, while potentially maintaining their individual mechanical, electrical, or optoelectronic functionality. In many instances, it is necessary to combine other material properties (e.g., an accessible band gap for active tuning[66] or ferroelectric response[67]) with the polaritonic behavior at a given frequency. For example, while AlN offers a Reststrahlen band that overlaps with the 8−12 μm atmospheric window, its 6 eV bandgap implies that free-carrier-based tuning methods[66] are impractical. However, one can envision active devices based on GaN/AlN SLs in which the accessible bandgap and controllable doping of GaN can enable free-carrier-based SPPs alongside the SPhP modes. In that case, the electromagnetic hybridization effect[20] and carrier injection could offer routes toward high-speed modulation of the XH polaritonic response.[66]

CONCLUSIONS

We have demonstrated the use of atomic-scale AlN/GaN SLs for creating hybrid optic phonon modes offering a distinct and tunable IR dielectric function. For layer thicknesses approaching the atomic scale, new phonon modes emerge such that the XHs IR properties are qualitatively different from their bulk components. This implies that the resulting SL does not behave as an effective medium composed of the two bulk materials, but rather as a XH material with its own distinct

phonon modes and IR response. We have shown the tunability of the XH optic phonons based on changes to the constituent layer thicknesses, with frequency shifts >10 cm^{-1}, and the emergence of new modes with only atomic-scale differences in the layer thickness required. This provides the opportunity to manipulate the IR response, including the frequencies of the polariton modes and control over the magnitude and dispersion in the IR optical constants, with less additional optical loss as compared to broadening the Reststrahlen band via carrier doping. The AlN/GaN XH has multiple, strongly anisotropic Reststrahlen bands, offering the potential for tailoring the spectral dispersion of both elliptical and hyperbolic spectral regions. The XH offers very large birefringence, with Δn in excess of unity over a large portion of the spectral range, reaching values >10. Such extremely large values of birefringence offer opportunities in a number of application spaces including on-chip optical elements, polarization control for waveguides, hyperlensing, and enhancing local emitters. In addition, the large birefringence of the XH makes it a promising material for probing the physics of propagating Dyakonov surface waves.[68] By manipulating the IR response, while maintaining other material parameters, XHs provide immense potential for multifunctional nanophotonic devices, for instance by layer-selective ultrafast modulation of the carrier densities. We believe that the implementation and further development of this XH approach will lead to significant advances in IR nanophotonic devices.

METHODS

Sample Growth. We used radio frequency (RF) plasma-assisted molecular beam epitaxy (MBE) to grow the polar epitaxial heterostructures on 3-in. diameter metal-polar semi-insulating 4H- and 6H-SiC substrates. The substrates were commercially polished using chemical-mechanical polishing to an epi-ready finish and were used as received. The reactive nitrogen was generated using an RF plasma source fed by ultrahigh purity N$_2$, which was further purified by an in-line purifier. The Ga and Al fluxes were generated using conventional dual-filament effusion cells. Other details about the MBE growth conditions were given in an earlier publication.[69] X-ray diffraction (XRD) measurements were carried out using a Rigaku system that employed a rotating Cu anode to produce Cu-Ka radiation. AlN/GaN SL thicknesses were estimated by fitting satellite peaks in XRD scans and high-resolution cross-sectional scanning transmission electron microscopy (STEM) images. The SL of Sample A was grown on ~50 nm AlN buffer layer. The SL consisted of 50 alternating layers of AlN and GaN and was fabricated with a thickness gradient across the SiC wr ranging from 2 nm to 3 nm for both, AlN and GaN layer thicknesses. For Sample B, there are 500 alternating layers of GaN and AlN, with average layer thicknesses of 1.35 ± 0.13 nm (4.78 monolayers) and 1.17 ± 0.05 nm (4.13 monolayers), respectively.

Electron Microscopy Preparation and Imaging. Cross-sectional STEM specimens were prepared as lift-out sections with an FEI Helios, a focused ion beam scanning electron microscope. Initial cuts were made at 30 kV, and final polishing was performed at 8 kV. STEM examination was carried out using a Nion UltraSTEM200-X operated at an accelerating voltage of 200 kV. Bright field, medium, and high-angle annular dark-field images were acquired. The image magnification calibration was verified each session using lattice measurements of evaporated gold nanoparticles.

Ellipsometry. Infrared ellipsometry was performed using a J.A. Woollam Mark II IR-VASE spectroscopic ellipsometer. The sample was mounted in the upright position and aligned using the standard four-quadrant detector to be positioned at the center of rotation. The broadband incident light was provided by a SiC glow-bar and was detected using a DLaTGS detector. The incident light was polarized

and detected using a polarizer and analyzer combination, and the various ratios of the p- and s-polarization components of the reflected light were plotted as Ψ and Δ, as is standard for ellipsometric measurements. The Ψ and Δ signals were both measured as a function of frequency (250–8000 cm^{-1}) at angles of incidence of 45, 55, 65, and 75° using the standard $\theta/2\theta$ geometry. The collected data were modeled using the WVASE software and based on the phonon frequencies extracted from the SHG measurements provided the starting parameters for the best fit. Following least-squares fitting, the resultant dielectric function was extracted.

Second Harmonic Spectroscopy. The second-harmonic phonon spectra[38,44] were obtained using an IR free-electron laser (FEL)[43] as a light source, which provided widely tunable, ~0.5% bandwidth laser pulses in the mid- to far-IR. Using a noncollinear autocorrelator geometry in reflection, both FEL beams were focused onto the SL wafer in spatial and temporal overlap, incident at angles $\alpha_1^i = 28°$ and $\alpha_2^i = 62°$, respectively. The SHG signal emerged spatially separated from the reflected fundamental beams and was detected using a LN$_2$-cooled mercury cadmium telluride (MCT) detector (InfraRed Associates). Both incoming beams as well as the detected SHG beam were p-polarized. Optical long- and short-pass filters were used in the incoming and detected beams, respectively, to suppress intrinsic higher harmonics of the FEL and scattered fundamental light. Simultaneously, the intensity of the reflected beam incident at $\alpha_2^i = 62°$ was recorded using a pyroelectric detector. Varying the FEL undulator gap allowed for tuning of the FEL center frequency ω, which thereby provided the SHG and reflectance spectra shown in Figure 2. Spectra were recorded at different locations on the SL wafer corresponding to varying absolute and relative thicknesses of the AlN and GaN layers, which were then extracted from XRD measurements for the representative examples shown in Figure 2. The full data set of the SHG spectra is provided in Figure S4 in the Supporting Information.

Otto-Geometry Measurements. Prism coupling in the Otto geometry was achieved using a triangular KRS5 ($n \approx 2.4$) prism in total internal reflection, which provided the in-plane momenta necessary to couple to SPhPs.[40] The prism was mounted on a motorized holder, which allowed for a controlled adjustment of the air gap width d, which was read out by white light interferometry,[60] see Figure 4a. The prism-sample assembly itself was mounted on a motorized rotation stage to vary the incidence angle θ_{ext}, and consequently the in-plane momentum $k = \omega/c\, n \sin \theta_{ext}$ of the incoming wave, thereby providing the means to excite SPhPs at different points along their dispersion. Scanning the FEL center frequency ω across the XH's Reststrahlen region while detecting the reflected intensity resulted in the reflectance spectra shown in Figure 4. The data were normalized to a reference spectrum taken at large air gaps ($d > 100\ \mu$m), where no light could be coupled to the SPhP modes. This measurement was repeated at various incidence angles θ_{ext}, and thus in-plane momenta k, to map out the polariton dispersion of the XH. Since multiple modes with different critical coupling behavior appear in the XH structure, the data shown in Figure 4 were recorded at a fixed air gap width of $d = 3.0\ \mu$m.

Transfer Matrix Calculations. The theoretical reflectance spectra in Figure 1 as well as the theoretical Otto geometry spectra in Figure 4 were acquired using a transfer matrix algorithm specifically accounting for absorptive anisotropic media.[37] The algorithm can treat an arbitrary number of layers, allowing to directly compare spectra for the XH and the explicit multilayer stack using the bulk dielectric functions of SiC, AlN, and GaN. The bulk parameters for SiC, AlN, and GaN are reported in Table S1 in the Supporting Information. The dispersion plots in Figure 5a and b were generated evaluating the reflection coefficient for p-polarized evanescent excitation ($k/k_0 > 1$) of the air/XH/SiC structure. The theoretical dispersion lines were extracted from the same type of calculations; however, with reduced damping of the XH by artificially lowering all phonon dampings by a factor of 5 in the parametrized dielectric function, see Supporting Information for details.

Optical Field Profiles. Simulations for Figure 5c–f were performed in CST studio suite[70] using the frequency domain solver.

To approximate Sample B within a finite 3D model, a unit cell with a height of 7.585 μm (585 nm of the XH material on top of 1 μm of SiC, with a 3 μm gap above and below) and in-plane dimensions of 21 μm (10 μm on either side of the dipole, with a 500 nm gap at the period edges) by 50 nm was chosen, which allow full directional propagation of the hyperbolic modes while minimizing nearest neighbor interactions. Unit cell boundaries were used at the in-plane edges of the substrate. Localized excitation of hyperbolic polaritons was facilitated by a port-mode dipole oriented normal to the sample (length 200 nm), placed 50 nm above the sample surface. The XH dielectric function with reduced damping was used for clarity.

Density Functional Perturbation Theory (DFPT). The Γ-point phonon frequencies were obtained using the first-principles approach as implemented in the Quantum-ESPRESSO package.[71] In this work, we used the generalized gradient approximation (GGA)[72] of Perdew–Burke–Ernzerhof (PBE)[73] for the exchange–correlation functional. The electronic wave functions were expanded in the plane wave basis set with a kinetic energy cutoff of 40 Ry. The Brillouin-zone was sampled with a grid of $18 \times 18 \times 2$ k-points according to the Monkhort-Pack method.[74] To compare theoretical results with those reported in the experiment, the GaN/AlN heterostructure was created using five monolayers of GaN and four monolayers of AlN. The geometry of the resultant structure was optimized and the phonon frequencies for the ground-state structure were calculated within DFPT.[75−78] Originating from long-ranged dipole–dipole interactions, the LO–TO splitting at the zone center ($\vec{q} \rightarrow 0$) was taken into account by including the nonanalytical contribution to the dynamical matrix.

ASSOCIATED CONTENT

Ⓢ Supporting Information

The Supporting Information is available free of charge on the ACS Publications website at DOI: 10.1021/acsnano.9b01275.

Details on IR ellipsometry data analysis, sample characterization by electron spectroscopy and microscopy, full SHG spectroscopy data set for sample A, DFPT calculations and results, discussion and calculations of XH polaritonic response, full data set of optical field profiles for polariton modes (PDF)

AUTHOR INFORMATION

Corresponding Authors
*E-mail: josh.caldwell@vanderbilt.edu.
*E-mail: alexander.paarmann@fhi-berlin.mpg.de.

ORCID Ⓞ
Daniel C. Ratchford: 0000-0001-7015-5305
Chase T. Ellis: 0000-0002-6718-6511
Nikolai C. Passler: 0000-0002-7477-8611
Rhonda M. Stroud: 0000-0001-5242-8015
Alexander Paarmann: 0000-0002-8271-2284
Joshua D. Caldwell: 0000-0003-0374-2168

Author Contributions

◆D.C.R. and C.J.W. contributed equally to this work. J.D.C., T.L.R., I.V., and J.G.T. originated the concept, while A.P. devised the SHG methods and Otto-configuration experiments. The manuscript was written by D.C.R., C.J.W., J.D.C., and A.P., with all authors assisting in the proof-reading and preparation for final submission. D.S.K. grew the samples, N.N. preformed XRD and AFM characterization, and M.T.H. performed XRD reciprocal space mapping and modeling. J.D.C., I.C., and A.J.G. performed the IR ellipsometry, while D.C.R. performed the least-squares fitting. SHG and Otto configuration measurements were performed by C.J.W., N.C.P., I.R., and A.P. Computations of the Otto-config-

REFERENCES

(1) Dai, S.; Ma, Q.; Andersen, T.; McLeod, A. S.; Fei, Z.; Liu, M. K.; Wagner, M.; Watanabe, K.; Taniguchi, T.; Thiemens, M.; Keilmann, F.; Jarillo-Herrero, P.; Fogler, M. M.; Basov, D. N. Subdiffractional Focusing and Guiding of Polaritonic Rays in a Natural Hyperbolic Material. *Nat. Commun.* **2015**, *6*, 6963.

(2) Li, P. N.; Lewin, M.; Kretinin, A. V.; Caldwell, J. D.; Novoselov, K. S.; Taniguchi, T.; Watanabe, K.; Gaussmann, F.; Taubner, T. Hyperbolic Phonon-Polaritons in Boron Nitride for Near-Field Optical Imaging and Focusing. *Nat. Commun.* **2015**, *6*, 7507.

(3) Liu, Z. W.; Lee, H.; Xiong, Y.; Sun, C.; Zhang, X. Far-Field Optical Hyperlens Magnifying Sub-Diffraction-Limited Objects. *Science* **2007**, *315*, 1685−1686.

(4) Taubner, T.; Korobkin, D.; Urzhumov, Y.; Shvets, G.; Hillenbrand, R. Near-Field Microscopy through a SiC Superlens. *Science* **2006**, *313*, 1594−1595.

(5) Autore, M.; Li, P.; Dolado, I.; Alfaro-Mozaz, F. J.; Esteban, R.; Atxabal, A.; Casanova, F.; Hueso, L. E.; Alonso-González, P.; Aizpurua, J.; Nikitin, A. Y.; Vélez, S.; Hillenbrand, R. Boron Nitride Nanoresonators for Phonon-Enhanced Molecular Vibrational Spectroscopy at the Strong Coupling Limit. *Light: Sci. Appl.* **2018**, *7*, 17172.

(6) Wang, T.; Li, P. N.; Chigrin, D. N.; Giles, A. J.; Bezares, F. J.; Glembocki, O. J.; Caldwell, J. D.; Taubner, T. Phonon-Polaritonic Bowtie Nanoantennas: Controlling Infrared Thermal Radiation at the Nanoscale. *ACS Photonics* **2017**, *4*, 1753−1760.

(7) Jackson, S. D. Towards High-Power Mid-Infrared Emission from a Fibre Laser. *Nat. Photonics* **2012**, *6*, 423−431.

(8) Adato, R.; Yanik, A. A.; Amsden, J. J.; Kaplan, D. L.; Omenetto, F. G.; Hong, M. K.; Erramilli, S.; Altug, H. Ultra-Sensitive Vibrational Spectroscopy of Protein Monolayers with Plasmonic Nanoantenna Arrays. *Proc. Natl. Acad. Sci. U. S. A.* **2009**, *106*, 19227−19232.

(9) Chatzakis, I.; Krishna, A.; Culbertson, J.; Sharac, N.; Giles, A. J.; Spencer, M. G.; Caldwell, J. D. Strong Confinement of Optical Fields Using Localized Surface Phonon Polaritons in Cubic Boron Nitride. *Opt. Lett.* **2018**, *43*, 2177−2180.

(10) Caldwell, J. D.; Glembocki, O. J.; Francescato, Y.; Sharac, N.; Giannini, V.; Bezares, F. J.; Long, J. P.; Owrutsky, J. C.; Vurgaftman, I.; Tischler, J. G.; Wheeler, V. D.; Bassim, N. D.; Shirey, L. M.; Kasica, R.; Maier, S. A. Low-Loss, Extreme Subdiffraction Photon Confinement *via* Silicon Carbide Localized Surface Phonon Polariton Resonators. *Nano Lett.* **2013**, *13*, 3690−3697.

(11) Caldwell, J. D.; Kretinin, A. V.; Chen, Y. G.; Giannini, V.; Fogler, M. M.; Francescato, Y.; Ellis, C. T.; Tischler, J. G.; Woods, C. R.; Giles, A. J.; Hong, M.; Watanabe, K.; Taniguchi, T.; Maier, S. A.; Novoselov, K. S. Sub-Diffractional Volume-Confined Polaritons in the Natural Hyperbolic Material Hexagonal Boron Nitride. *Nat. Commun.* **2014**, *5*, 5221.

(12) Caldwell, J. D.; Lindsay, L.; Giannini, V.; Vurgaftman, I.; Reinecke, T. L.; Maier, S. A.; Glembocki, O. J. Low-Loss, Infrared and Terahertz Nanophotonics Using Surface Phonon Polaritons. *Nanophotonics* **2015**, *4*, 44−68.

(13) Dai, S.; Fei, Z.; Ma, Q.; Rodin, A. S.; Wagner, M.; McLeod, A. S.; Liu, M. K.; Gannett, W.; Regan, W.; Watanabe, K.; Taniguchi, T.; Thiemens, M.; Dominguez, G.; Neto, A. H. C.; Zettl, A.; Keilmann, F.; Jarillo-Herrero, P.; Fogler, M. M.; Basov, D. N. Tunable Phonon Polaritons in Atomically Thin van der Waals Crystals of Boron Nitride. *Science* **2014**, *343*, 1125−1129.

(14) Greffet, J. J.; Carminati, R.; Joulain, K.; Mulet, J. P.; Mainguy, S. P.; Chen, Y. Coherent Emission of Light by Thermal Sources. *Nature* **2002**, *416*, 61−64.

(15) Hillenbrand, R.; Taubner, T.; Keilmann, F. Phonon-Enhanced Light-Matter Interaction at the Nanometre Scale. *Nature* **2002**, *418*, 159−162.

(16) Wang, T.; Li, P. N.; Hauer, B.; Chigrin, D. N.; Taubner, T. Optical Properties of Single Infrared Resonant Circular Microcavities for Surface Phonon Polaritons. *Nano Lett.* **2013**, *13*, 5051−5055.

(17) Khurgin, J. B. How to Deal with the Loss in Plasmonics and Metamaterials. *Nat. Nanotechnol.* **2015**, *10*, 2−6.

(18) Khurgin, J. B. Relative Merits of Phononics Vs. Plasmonics: The Energy Balance Approach. *Nanophotonics* **2018**, *7*, 305−316.

(19) Gubbin, C. R.; De Liberato, S. Theory of Four-Wave-Mixing in Phonon Polaritons. *ACS Photonics* **2018**, *5*, 284−288.

(20) Caldwell, J. D.; Vurgaftman, I.; Tischler, J. G.; Glembocki, O. J.; Owrutsky, J. C.; Reinecke, T. L. Atomic-Scale Photonic Hybrids for Mid-Infrared and Terahertz Nanophotonics. *Nat. Nanotechnol.* **2016**, *11*, 9−15.

(21) Folland, T. G.; Caldwell, J. D. *Semiconductor Nanophotonics Using Surface Polaritons, Quantum Nano-Photonics*; Di Bartolo, B., Silvestri, L., Cesaria, M., Collins, J., Eds.; Springer Netherlands: Dordrecht, 2018; pp 235−254.

(22) Yu, P. Y.; Cardona, M. *Fundamentals of Semiconductors*; Springer: 2010; Vol. 4.

(23) Paudel, T. R.; Lambrecht, W. R. L. Computational Study of Phonon Modes in Short-Period AlN/GaN Superlattices. *Phys. Rev. B: Condens. Matter Mater. Phys.* **2009**, *80*, 104202.

(24) Enderlein, R.; Suisky, D.; Röseler, J. Optical Phonons in Superlattices. *Phys. Status Solidi B* **1991**, *165*, 9−66.

(25) Caldwell, J. D.; Novoselov, K. S. Mid-Infrared Nanophotonics. *Nat. Mater.* **2015**, *14*, 364−365.

(26) Ma, W.; Alonso-González, P.; Li, S.; Nikitin, A. Y.; Yuan, J.; Martín-Sánchez, J.; Taboada-Gutiérrez, J.; Amenabar, I.; Li, P.; Vélez, S.; Tollan, C.; Dai, Z.; Zhang, Y.; Sriram, S.; Kalantar-Zadeh, K.; Lee, S.-T.; Hillenbrand, R.; Bao, Q. In-Plane Anisotropic and Ultra-Low-Loss Polaritons in a Natural van der Waals Crystal. *Nature* **2018**, *562*, 557−562.

(27) Poddubny, A.; Iorsh, I.; Belov, P.; Kivshar, Y. Hyperbolic Metamaterials. *Nat. Photonics* **2013**, *7*, 948.

(28) Azuhata, T.; Sota, T.; Suzuki, K.; Nakamura, S. Polarized Raman Spectra in GaN. *J. Phys.: Condens. Matter* **1995**, *7*, L129−L133.

(29) McNeil, L. E.; Grimsditch, M.; French, R. H. Vibrational Spectroscopy of Aluminum Nitride. *J. Am. Ceram. Soc.* **1993**, *76*, 1132−1136.

(30) Jusserand, B.; Cardona, M. Raman Spectroscopy of Vibrations in Superlattices. In *Light Scattering in Solids V: Superlattices and Other Microstructures*; Cardona, M., Güntherodt, G., Eds.; Springer Berlin Heidelberg: Berlin, Heidelberg, 1989; pp 49−152.

(31) Gleize, J.; Demangeot, F.; Frandon, J.; Renucci, M. A.; Widmann, F.; Daudin, B. Phonons in a Strained Hexagonal GaN-AlN Superlattice. *Appl. Phys. Lett.* **1999**, *74*, 703−705.

(32) Gleize, J.; Renucci, M. A.; Frandon, J.; Demangeot, F. Anisotropy Effects on Polar Optical Phonons in Wurtzite GaN/AlN Superlattices. *Phys. Rev. B: Condens. Matter Mater. Phys.* **1999**, *60*, 15985−15992.

(33) MacMillan, M. F.; Devaty, R. P.; Choyke, W. J.; Asif Khan, M.; Kuznia, J. Infrared Reflectance of AlN-GaN Short Period Superlattice Films. *J. Appl. Phys.* **1996**, *80*, 2372−2377.

(34) Smirnov, M. B.; Karpov, S. V.; Davydov, V. Y.; Smirnov, A. N.; Zavarin, E. E.; Lundin, V. V. Vibrational Spectra of AlN/GaN Superlattices: Theory and Experiment. *Phys. Solid State* **2005**, *47*, 742−753.

(35) Schubert, M. *Infrared Ellipsometry on Semiconductor Layer Structures: Phonons, Plasmons, and Polaritons*; Springer: Heidelberg, 2004; Vol. *209*.

(36) Schubert, M.; Hofmann, T.; Šik, J. Long-Wavelength Interface Modes in Semiconductor Layer Structures. *Phys. Rev. B: Condens. Matter Mater. Phys.* **2005**, *71*, 035324.

(37) Passler, N. C.; Paarmann, A. Generalized 4 × 4 Matrix Formalism for Light Propagation in Anisotropic Stratified Media: Study of Surface Phonon Polaritons in Polar Dielectric Heterostructures. *J. Opt. Soc. Am. B* **2017**, *34*, 2128−2139.

(38) Paarmann, A.; Razdolski, I.; Gewinner, S.; Schöllkopf, W.; Wolf, M. Effects of Crystal Anisotropy on Optical Phonon Resonances in Midinfrared Second Harmonic Response of SiC. *Phys. Rev. B: Condens. Matter Mater. Phys.* **2016**, *94*, 134312.

(39) Paarmann, A.; Razdolski, I.; Melnikov, A.; Gewinner, S.; Schöllkopf, W.; Wolf, M. Second Harmonic Generation Spectroscopy in the Reststrahl Band of SiC Using an Infrared Free-Electron Laser. *Appl. Phys. Lett.* **2015**, *107*, 081101.

(40) Passler, N. C.; Razdolski, I.; Gewinner, S.; Schollkopf, W.; Wolf, M.; Paarmann, A. Second-Harmonic Generation from Critically Coupled Surface Phonon Polaritons. *ACS Photonics* **2017**, *4*, 1048−1053.

(41) Razdolski, I.; Chen, Y. G.; Giles, A. J.; Gewinner, S.; Schollkopf, W.; Hong, M. H.; Wolf, M.; Giannini, V.; Caldwell, J. D.; Maier, S. A.; Paarmann, A. Resonant Enhancement of Second-Harmonic Generation in the Mid-Infrared Using Localized Surface Phonon Polaritons in Subdiffractional Nanostructures. *Nano Lett.* **2016**, *16*, 6954−6959.

(42) Gubbin, C. R.; De Liberato, S. Theory of Nonlinear Polaritonics: $\chi^{(2)}$ Scattering on a β-SiC Surface. *ACS Photonics* **2017**, *4*, 1381−1388.

(43) Schöllkopf, W.; Gewinner, S.; Junkes, H.; Paarmann, A.; von Helden, G.; Bluem, H.; Todd, A. M. M. In *The New IR and Thz FEL Facility at the Fritz Haber Institute in Berlin*; SPIE Optics + Optoelectronics 2015, Prague, Czech Republic, 2015.

(44) Winta, C. J.; Gewinner, S.; Schöllkopf, W.; Wolf, M.; Paarmann, A. Second-Harmonic Phonon Spectroscopy of α-Quartz. *Phys. Rev. B: Condens. Matter Mater. Phys.* **2018**, *97*, 094108.

(45) Berreman, D. W. Infrared Absorption at Longitudinal Optic Frequency in Cubic Crystal Films. *Phys. Rev.* **1963**, *130*, 2193−2198.

(46) Campione, S.; Brener, I.; Marquier, F. Theory of Epsilon-near-zero Modes in Ultrathin Films. *Phys. Rev. B: Condens. Matter Mater. Phys.* **2015**, *91*, 121408.

(47) Vassant, S.; Hugonin, J. P.; Marquier, F.; Greffet, J. J. Berreman Mode and Epsilon near Zero Mode. *Opt. Express* **2012**, *20*, 23971−23977.

(48) Passler, N. C.; Razdolski, I.; Katzer, D. S.; Storm, D. F.; Caldwell, J. D.; Wolf, M.; Paarmann, A. Resonant Field Enhancement of Epsilon Near Zero Berreman Modes in an Ultrathin AlN Film. *arXiv:1811.10370*, 2018. https://arxiv.org/abs/1811.10370 (accessed May 29, 2019).

(49) Darakchieva, V.; Valcheva, E.; Paskov, P. P.; Schubert, M.; Paskova, T.; Monemar, B.; Amano, H.; Akasaki, I. Phonon Mode Behavior in Strained Wurtzite AlN/GaN Superlattices. *Phys. Rev. B: Condens. Matter Mater. Phys.* **2005**, *71*, 115329.

(50) Goñi, A. R.; Siegle, H.; Syassen, K.; Thomsen, C.; Wagner, J. M. Effect of Pressure on Optical Phonon Modes and Transverse Effective Charges in GaN and AlN. *Phys. Rev. B: Condens. Matter Mater. Phys.* **2001**, *64*, 035205.

(51) Gorczyca, I.; Christensen, N. E.; Peltzer y Blancá, E. L.; Rodriguez, C. O. Optical Phonon Modes in GaN and AlN. *Phys. Rev. B: Condens. Matter Mater. Phys.* **1995**, *51*, 11936−11939.

(52) Polian, A.; Grimsditch, M.; Grzegory, I. Elastic Constants of Gallium Nitride. *J. Appl. Phys.* **1996**, *79*, 3343−3344.

(53) Kirk, C. T. Quantitative Analysis of the Effect of Disorder-Induced Mode Coupling on Infrared Absorption in Silica. *Phys. Rev. B: Condens. Matter Mater. Phys.* **1988**, *38*, 1255−1273.

(54) *WVASE*; J. A. Woollam, 2019. https://www.jawoollam.com/ellipsometry-software/wvase (accessed May 29, 2019).

(55) Harima, H.; Nakashima, S. i.; Uemura, T. Raman Scattering from Anisotropic LO-Phonon−Plasmon−Coupled Mode in *n*-Type 4H− and 6H−SiC. *J. Appl. Phys.* **1995**, *78*, 1996−2005.

(56) Niu, S.; Joe, G.; Zhao, H.; Zhou, Y.; Orvis, T.; Huyan, H.; Salman, J.; Mahalingam, K.; Urwin, B.; Wu, J.; Liu, Y.; Tiwald, T. E.; Cronin, S. B.; Howe, B. M.; Mecklenburg, M.; Haiges, R.; Singh, D. J.; Wang, H.; Kats, M. A.; Ravichandran, J. Giant Optical Anisotropy in a Quasi-One-Dimensional Crystal. *Nat. Photonics* **2018**, *12*, 392−396.

(57) Folland, T. G.; Caldwell, J. D. Precise Control of Infrared Polarization Using Crystal Vibrations. *Nature* **2018**, *562*, 499−501.

(58) Falge, H. J.; Otto, A. Dispersion of Phonon-Like Surface Polaritons on α-Quartz Observed by Attenuated Total Reflection. *Phys. Status Solidi B* **1973**, *56*, 523−534.

(59) Neuner, B.; Korobkin, D.; Fietz, C.; Carole, D.; Ferro, G.; Shvets, G. Critically Coupled Surface Phonon-Polariton Excitation in Silicon Carbide. *Opt. Lett.* **2009**, *34*, 2667−2669.

(60) Pufahl, K.; Passler, N. C.; Grosse, N. B.; Wolf, M.; Woggon, U.; Paarmann, A. Controlling Nanoscale Air-Gaps for Critically Coupled Surface Polaritons by Means of Non-Invasive White-Light Interferometry. *Appl. Phys. Lett.* **2018**, *113*, 161103.

(61) Passler, N. C.; Gubbin, C. R.; Folland, T. G.; Razdolski, I.; Katzer, D. S.; Storm, D. F.; Wolf, M.; De Liberato, S.; Caldwell, J. D.; Paarmann, A. Strong Coupling of Epsilon-Near-Zero Phonon Polaritons in Polar Dielectric Heterostructures. *Nano Lett.* **2018**, *18*, 4285−4292.

(62) Runnerstrom, E. L.; Kelley, K. P.; Folland, T. G.; Nolen, J. R.; Engheta, N.; Caldwell, J. D.; Maria, J.-P. Polaritonic Hybrid-Epsilon-near-Zero Modes: Beating the Plasmonic Confinement Vs Propagation-Length Trade-Off with Doped Cadmium Oxide Bilayers. *Nano Lett.* **2019**, *19*, 948−957.

(63) Caldwell, J. D.; Aharonovich, I.; Cassabois, G.; Edgar, J. H. G. B.; Basov, D. N. Photonics with Hexagonal Boron Nitride. *Nat. Mater.* **2019**, in press.

(64) Giles, A. J.; Dai, S. Y.; Glembocki, O. J.; Kretinin, A. V.; Sun, Z. Y.; Ellis, C. T.; Tischler, J. G.; Taniguchi, T.; Watanabe, K.; Fogler, M. M.; Novoselov, K. S.; Basov, D. N.; Caldwell, J. D. Imaging of Anomalous Internal Reflections of Hyperbolic Phonon-Polaritons in Hexagonal Boron Nitride. *Nano Lett.* **2016**, *16*, 3858−3865.

(65) Ishii, S.; Kildishev, A. V.; Narimanov, E.; Shalaev, V. M.; Drachev, V. P. Sub-Wavelength Interference Pattern from Volume Plasmon Polaritons in a Hyperbolic Medium. *Laser Photon Rev.* **2013**, *7*, 265−271.

(66) Dunkelberger, A. D.; Ellis, C. T.; Ratchford, D. C.; Giles, A. J.; Kim, M.; Kim, C. S.; Spann, B. T.; Vurgaftman, I.; Tischler, J. G.; Long, J. P.; Glembocki, O. J.; Owrutsky, J. C.; Caldwell, J. D. Active Tuning of Surface Phonon Polariton Resonances *via* Carrier Photoinjection. *Nat. Photonics* **2018**, *12*, 50−56.

(67) Beechem, T. E.; Goldflam, M. D.; Sinclair, M. B.; Peters, D. W.; McDonald, A. E.; Paisley, E. A.; Kitahara, A. R.; Drury, D. E.; Burckel, D. B.; Finnegan, P. S.; Kim, J.-W.; Choi, Y.; Ryan, P. J.; Ihlefeld, J. F. Tunable Infrared Devices *via* Ferroelectric Domain Reconfiguration. *Adv. Opt. Mater.* **2018**, *6*, 1800862.

(68) Dyakonov, M. I. New Type of Electromagnetic Wave Propagating at an Interface. *Soviet Physics JETP* **1988**, *67*, 714−716.

(69) Katzer, D. S.; Meyer, D. J.; Storm, D. F.; Nepal, N.; Wheeler, V. D. Silicon Nitride Thin Films Deposited Using Electron-Beam Evaporation in an RF Plasma MBE System. *J. Vac. Sci. Technol., B: Nanotechnol. Microelectron.: Mater., Process., Meas., Phenom.* **2014**, *32*, 02C117.

(70) *CST, CST Studio Suite*; Dassault Systems, 2019. https://www.cst.com/products/csts2 (accessed May 29, 2019).

(71) Giannozzi, P.; Baroni, S.; Bonini, N.; Calandra, M.; Car, R.; Cavazzoni, C.; Ceresoli, D.; Chiarotti, G. L.; Cococcioni, M.; Dabo, I.; Dal Corso, A.; De Gironcoli, S.; Fabris, S.; Fratesi, G.; Gebauer, R.; Gerstmann, U.; Gougoussis, C.; Kokalj, A.; Lazzeri, M.; Martin-Samos, L.; Marzari, N.; Mauri, F.; Mazzarello, R.; Paolini, S.; Pasquarello, A.; Paulatto, L.; Sbraccia, C.; Scandolo, S.; Sclauzero, G.; Seitsonen, A. P.; Smogunov, A.; Umari, P.; Wentzcovitch, R. M. Quantum Espresso: A Modular and Open-Source Software Project for Quantum Simulations of Materials. *J. Phys.: Condens. Matter* **2009**, *21*, 395502.

(72) Perdew, J. P.; Yue, W. Accurate and Simple Density Functional for the Electronic Exchange Energy: Generalized Gradient Approximation. *Phys. Rev. B: Condens. Matter Mater. Phys.* **1986**, *33*, 8800−8802.

(73) Perdew, J. P.; Burke, K.; Ernzerhof, M. Generalized Gradient Approximation Made Simple. *Phys. Rev. Lett.* **1996**, *77*, 3865−3868.

(74) Monkhorst, H. J.; Pack, J. D. Special Points for Brillouin-Zone Integrations. *Phys. Rev. B* **1976**, *13*, 5188−5192.

(75) Baroni, S.; De Gironcoli, S.; Dal Corso, A.; Giannozzi, P. Phonons and Related Crystal Properties from Density-Functional Perturbation Theory. *Rev. Mod. Phys.* **2001**, *73*, 515−562.

(76) Baroni, S.; Giannozzi, P.; Testa, A. Greens-Function Approach to Linear Response in Solids. *Phys. Rev. Lett.* **1987**, *58*, 1861−1864.

(77) Giannozzi, P.; De Gironcoli, S.; Pavone, P.; Baroni, S. *Ab Initio* Calculation of Phonon Dispersions in Semiconductors. *Phys. Rev. B: Condens. Matter Mater. Phys.* **1991**, *43*, 7231−7242.

(78) Gonze, X. Adiabatic Density-Functional Perturbation Theory. *Phys. Rev. A: At., Mol., Opt. Phys.* **1995**, *52*, 1096−1114.